IRIS AperTO

UNIVERSITÀ DEGLI STUDI DI TORINO

AperTO - Archivio Istituzionale Open Access dell'Università di Torino

Surface and structural characterization of Cu-exchanged hydroxyapatites and their application in H2O2 electrocatalytic reduction

This is the author's manuscript

Original Citation:

Availability:

This version is available http://hdl.handle.net/2318/1869719 since 2022-07-17T14:03:59Z

Published version:

DOI:10.1016/j.apsusc.2022.153495

Terms of use:

Open Access

Anyone can freely access the full text of works made available as "Open Access". Works made available under a Creative Commons license can be used according to the terms and conditions of said license. Use of all other works requires consent of the right holder (author or publisher) if not exempted from copyright protection by the applicable law.

(Article begins on next page)

26 December 2024

Surface and structural characterization of Cu-exchanged hydroxyapatites and their application in H_2O_2 electrocatalytic reduction

Guillermo Escolano Casado[a], Pavlo Ivanchenko[a,b], Geo Paul[c], Chiara Bisio[c,d], Leonardo Marchese[c], Amir M. Ashrafi[e], Vedran Milosavljevic[e,f], Lorenzo Degli Esposti[g], Michele Iafisco[g] and Lorenzo Mino[a]*

[a]Department of Chemistry and Interdepartmental Centre NIS, University of Torino, Via Giuria 7, 10125 Torino, Italy
[b]Mobility, Logistics and Automotive Technology Research Center, Vrije Universiteit Brussels, Pleinlaan 2, Brussels 1050, Belgium
[c]Dipartimento di Scienze e Innovazione Tecnologica, Università degli Studi del Piemonte Orientale "Amedeo Avogadro", Viale Teresa Michel 11, 15121 Alessandria, Italy
[d] CNR-SCITEC Istituto di Scienze e Tecnologie Chimiche "G. Natta", Via C. Golgi 19, 20133-Milano, Italy
[e]Department of Chemistry and Biochemistry, Mendel University in Brno, Zemedelska 1665/1, CZ-61300 Brno, Czech Republic
[f]Central European Institute of Technology, Brno University of Technology, Purkynova 123, CZ-61200, Brno, Czech Republic
[g]Institute of Science and Technology for Ceramics (ISTEC), National Research Council (CNR), Via Granarolo 64, 48018 Faenza, Italy
*Corresponding author email address: lorenzo.mino@unito.it

Dedication. To the memory of our unforgettable colleague, mentor and friend, Gianmario Martra, too early passed away, who constantly inspired this research activity.

Abstract

We report on the preparation of hydroxyapatite (HA) nanoparticles with high specific surface area, terminated with calcium-rich {010} facets, and their subsequent surface functionalization with copper by cationic exchange with copper nitrate solutions at different concentrations. Elemental analysis highlighted a progressive increase of the amount of copper incorporated into the HA, reaching a maximum of ~ 7 wt%. A combined X-ray diffraction and solid-state NMR investigation showed no significant structural differences after the Cu functionalization, confirming that the copper exchange occurs mainly at the surface until saturation and, for the higher Cu concentrations, also in the sub-surface/bulk layers of the material, without altering the HA crystal structure. The gradual substitution of surface Ca^{2+} by Cu^{2+} was studied also by IR spectroscopy using carbon monoxide as probe molecule. Finally, we assessed the catalytic activity of the materials testing the electrochemical reduction of H_2O_2 by cyclic voltammetry. We observed a progressive increase in catalytic activity correlated with the amount of Cu, suggesting the possible application of copper-exchanged HA as electrochemical H_2O_2 sensors.

Keywords: copper-exchanged hydroxyapatites, FTIR spectroscopy, solid-state NMR, electrochemical H_2O_2 sensors, electrocatalysis.

1. Introduction

Hydroxyapatite (HA) [$Ca_{10}(PO_4)_6(OH)_2$] is the principal constituent of the mineralised part of the human body (bones and teeth). It is a ceramic material which has an intrinsic biocompatibility and it is considered an important bioactive and bioresorbable biomaterial [1, 2]. However, the importance of the HAs is not only restricted to study how they formed in the human body or to their uses for biomedical applications but, recently, synthetic HAs have gained a great interest due to their applications in many different fields such as heterogeneous catalysis [3], agriculture [4, 5], and pollution remediation [6].

An important property to consider is the structure of the HAs and their surface terminations, which can be tailored by specific synthesis conditions [7]. From this point of view, the HAs are composed of layers stacked along the [010] crystallographic direction following the sequence -ABA-ABA-ABA-, where A = $Ca_3(PO_4)_2$ and B = $Ca_4(PO_4)_2(OH)_2$. Both layers deviate from stoichiometric Ca/P molar ratio of HA (1.67) since A layer has a Ca/P ratio of 1.5 and B layer has a ratio of 2. There are three possible {010} surface terminations for the HAs [7]: (i) the …-ABA-ABA stoichiometric arrangement; (ii) the (010)_Ca-rich …-ABA-AB; (iii) {010} the (010)_P-rich …-ABA-A. The latter two non-stoichiometric surfaces can coexist on HAs particles [8].

The morphology of the HAs is another important parameter for the improvement and fine tuning of their applications. The most common morphologies of synthetic HA nanoparticles are rod-like and plate-like, and the latter is the same observed in bone tissue HA [9]. In both cases, the prevailing surface terminations are of {010} type [7, 10]. The different morphologies can result in significantly different functional behaviors as highlighted, for instance, for biomolecules adsorption [11] and for methane oxidation reactions [12].

Concerning the use of HAs in catalysis, the synthesis methodology is usually tailored to produce HAs in nanometric size with a high specific surface area, which can be effectively exploited for the desired chemical reactions [3]. Moreover, the excellent capacity of HAs to exchange their surface ions with other ions similar in charge and volume can be extremely useful to tune their catalytic properties. Indeed, the $(PO_4)^{3-}$ anions can be substituted by $(VO_4)^{3-}$, $(AsO_4)^{3-}$, $(HPO_4)^{2-}$, $(CO_3)^{2-}$ or $(SO_4)^{2-}$, while the Ca^{2+} cations can be exchanged by divalent cations such as Mg^{2+}, Cu^{2+}, Sr^{2+}, Mn^{2+}, Fe^{2+} etc [6]. In particular, copper-exchanged HAs have been tested for different applications, including selective hydrogenations [13], formaldehyde oxidation [14], azide–alkyne cycloadditions [15], NO_x selective catalytic reduction [16, 17] and antimicrobial applications [18]. Different synthetic strategies have been explored to insert Cu in the HA structure based on ion exchange procedures with copper salts or co-precipitation methods [14, 19]. Different bulk locations for Cu^{2+} ions in the HA structure have been reported, including bulk Ca^{2+} substitution (causing a decrease of the cell parameters due to its smaller ionic radius) and hydrogen substitution in structural hydroxyls forming oxocuprate ions (causing an increase of the cell parameters)

[20, 21]. For catalysis application is particularly interesting to obtain a copper doping onto the surface of HA, which has been achieved through ion exchange with surface Ca^{2+} ions, by depositing a copper-containing amorphous layer onto HA surface, and also by surface complexation [22].

In this work we present the preparation of HA nanoparticles with high specific surface area, elongated along their crystallographic *c*-axis, and, thus, preferentially exposing {010} facets. Taking advantage of the intrinsic characteristic of the HA as ion-exchanger and its high surface concentration of Ca^{2+} ions, the synthesized HA was then surface-functionalized with Cu^{2+} by ion exchange between the surface Ca^{2+} and Cu^{2+} cations through soaking in a copper (II) solution. HA synthesis was tailored to produce nanocrystals with high surface concentration of Ca^{2+} ions as well as high reactivity by limiting its crystallization, thus being particularly suitable for surface ion exchange. Different concentrations of copper were tested, until the maximum exchange capacity of the HA was reached. The obtained materials were characterized in terms of specific surface area (SSA), elemental composition by inductively coupled plasma-optical emission spectrometry (ICP-OES) and structural properties by combining X-ray powder diffraction (PXRD) and solid state Nuclear Magnetic Resonance (ss-NMR). The surface sites of the materials were investigated by Fourier transform Infrared (FTIR) spectroscopy of adsorbed probe molecules, using carbon monoxide (CO) since this molecule is sensitive to both Ca^{2+} and Cu^{2+} cations. Finally, a preliminary test of the electrocatalytic activity of the material was performed. Indeed, functionalized HA have been largely exploited to realize electrochemical sensors, especially for analytes of biomedical interest [23-25]. In our study we have assessed for the first time by cyclic voltammetry the catalytic activity of copper-exchanged HAs toward the electrochemical reduction of H_2O_2, which is a crucial testing molecule and a side product of several biochemical reactions [26]. The presence of copper is expected to enhance the catalytic activity toward hydrogen peroxide reduction, as already observed in other systems [27], possibly allowing the future development of electrochemical H_2O_2 sensors based on these materials.

2. Experimental

2.1 Sample synthesis

Calcium hydroxide ($Ca(OH)_2$, ≥ 95.0% pure), phosphoric acid (H_3PO_4, 80% pure), and copper (II) nitrate hemi(penta-hydrate) ($Cu(NO_3)_2 \cdot 2.5H_2O$, ≥ 99.99% pure) were purchased from Sigma-Aldrich and used without further purification. All the solutions were prepared with double distilled water. The hydroxyapatites nanoparticles enriched with calcium at the {010} facets (hereafter HA) were synthesized as reported in a previous publication [7], by a co-precipitation method using a H_3PO_4 solution (1.26 M, 0.225 L) which was added dropwise into a $Ca(OH)_2$ solution (1.35 M, 0.375 L) under stirring with a flux rate of 1 drop/second. The reaction solution was left under stirring for 24 hours. The initial pH of the

$Ca(OH)_2$ solution was 12.8 and it decreased to 12.6 after H_3PO_4 addition. After 24 hours of maturation, the final pH was 12.1. The temperature was kept at 310 K throughout all the synthesis process. Subsequently, the powders were recovered by centrifugation of the mother liquor (4500 RPM, 5 min), washed with distilled water three times, and, finally, dried using a freeze-dryer. Afterward, HA dry powder was ground and fractioned employing 75 µm sieves.

Copper-exchanged HA samples were prepared by suspending 1.5 g of HA into 50 mL of copper (II) nitrate solution under stirring at room temperature for 15 minutes [16]. Longer contact times, up to 60 minutes, do not improve significantly the final copper uptake (see Table S1 in the supplementary material). Afterwards, a washing and freeze-drying procedure was carried out on all samples as described above. Three different initial concentrations of copper nitrate solution were used: 0.01 M, 0.05 M and 0.1 M, resulting in three different copper-exchanged samples, which were called as HA_Cu_0.01, HA_Cu_0.05, and HA_Cu_0.1, respectively. The initial pH of the copper nitrate solutions was 4.8, 4.3 and 4.0, while the final pH after the exchange procedure was 6.8, 4.6 and 4.3 for the HA_Cu_0.01, HA_Cu_0.05, and HA_Cu_0.1, respectively. At the employed acid pH, the ζ-potential of HA was slightly negative (i.e. -2.9 ± 1.3 mV at pH = 4.8 and -4.0 ± 0.2 mV at pH = 4.0), suggesting that it could interact with the positively charged Cu^{2+} cations in all tested conditions. As control of ion exchange, 1.5 g of HA was suspended into 50 mL of acidic water at pH 4.8 or 4.0 under stirring at room temperature for 15 or 60 minutes. Copper-exchange procedure was performed at least in triplicate in order to verify the repeatability of the process.

2.2 Characterization techniques

2.2.1 Elemental analysis. The elemental analysis of the samples as well as quantification of ion exchange was performed by Inductively Coupled Plasma-Optical Emission Spectrometry (ICP-OES) using an Agilent 5100 spectrometer (Agilent Technologies, Santa Clara, CA, USA). Sample preparation consisted in dissolving 10 mg of the powdered samples in 50 mL of a 1 wt.% HNO_3 aqueous solution in triplicate. In the case of ion exchange experiment, the supernatant collected after exchange was diluted with 1 wt.% HNO_3 aqueous solution before analysis. Quantification of Ca, P, and Cu content was made by calibration curves prepared from commercial certified standard solutions (Sigma Aldrich, St. Luis, MO, USA). The results are expressed as the mean and standard deviation of triplicate analysis.

2.2.2 Specific surface area. The SSA was determined with a Micromeritics ASAP 2020 by nitrogen adsorption at 77 K applying the Brunauer-Emmett-Teller (BET) model. Before performing the measurements, the powders were outgassed at room temperature for 12 hours.

2.2.3 ζ -potential measurements. ζ-Potential of the samples was measured with a Zetasizer Nano ZSP analyser (Malvern, UK). The samples were dispersed in aqueous acidic solution at pH 4.0 or pH 4.8 at a concentration of 0.5 mg mL^{-1}, and the ζ-potential was measured using a DTS1061 cell (Malvern, UK) at 25 °C. Three measurements (maximum of 100 runs each) were collected for each sample and the results are expressed as their mean and standard deviation.

2.2.4 X-ray diffraction. XRD patterns of the powders were collected with an PANalytical X'Pert Pro powder diffractometer equipped with X'Celerator detector using Cu Kα radiation generated at 40 kV and 45 mA. The instrument was configured with ¼ and ¼ slits. A quartz sample holder was used. A 2θ range from 10° to 90° with a step size (°2θ) of 0.02 and a counting time of 90 seconds per point was used. PXRD Rietveld refinement analysis was performed with the software TOPAS5. For all refinements, tabulated HA atomic coordinates were used as initial model and anisotropic peak-broadening effects due to the anisotropic crystal shape were modeled using symmetrized spherical harmonics, while the pattern's background was modeled as 11^{th} order Chebychev function. The unit cell parameters and average sizes of crystalline domains along the hydroxyapatite axis directions $D_{(002)}$ and $D_{(310)}$ were calculated with the software TOPAS5 as full-profile peak broadening evaluation. The instrumental contribution to peak broadening was evaluated by collecting the PXRD pattern of a LaB_6 standard sample. The standard deviations of the unit cell parameters and average sizes of crystalline domains were automatically calculated by the software.

2.2.5 Solid-State Nuclear Magnetic Resonance. Solid-state NMR spectra were acquired on a Bruker Avance III 500 spectrometer and a wide bore 11.75 Tesla magnet with operational frequencies for ^{1}H and ^{31}P of 500.13 and 202.45 MHz, respectively. A 4 mm triple resonance probe, in double resonance mode, with MAS was employed in all the experiments and the samples were packed in a zirconia rotor and spun at a MAS rate of 15 kHz, giving a sample temperature of 304 K. The ^{31}P MAS spectra were acquired with a 90-degree pulse and the magnitude of the radio frequency field was 71 kHz with ^{1}H decoupling during acquisition. For the ^{31}P $\{^{1}H\}$ cross polarization (CP) MAS experiments, the proton radio frequencies (RF) of 100 and 50 kHz were used for initial excitation and decoupling, respectively. During the CP period, the ^{1}H RF field was ramped using 100 increments, whereas the ^{31}P RF field was maintained at a constant level. During acquisition, the protons were decoupled from ^{31}P using a Spinal64 decoupling scheme. A moderate ramped RF field of 55 kHz was used for spin locking, while the ^{31}P RF field was matched to obtain optimal signal. A CP contact time of 6 ms was used. ^{1}H MAS NMR spectra were collected with an excitation pulse of 100 kHz. In addition, a rotor-synchronized spin-echo sequence (π/2–τ–π–τ–acquisition) was also applied to record the ^{1}H NMR spectra with delay time of 2000 ms. The relaxation delays, d1, between accumulations were 100 s for ^{31}P and 5 s for ^{1}H. All chemical shifts are

reported using δ scale and are externally referenced to ammonium dihydrogen phosphate at 0.8 ppm for ^{31}P and tetramethylsilane at 0 ppm for ^{1}H.

2.2.6 IR spectroscopy. For FTIR measurements, the powders were pressed into self-supporting pellets and placed in quartz IR cells, equipped with KBr windows, designed to perform spectroscopic measurements at low temperature (ca. 100 K, by cooling with liquid N_2). The cell was connected to a conventional vacuum line (residual pressure = 1×10^{-3} mbar) to perform *in situ* all thermal treatments and adsorption-desorption experiments. All the samples were pre-outgassed at 423 K in order to remove all the water molecules in direct contact with the surface (this temperature was found to be a compromise allowing to remove the irreversibly adsorbed water without causing any changes in the material structure) [7]. The pressure of 50 mbar of CO was admitted inside the cell with the pre-treated material subsequently cooled down to ca. 100 K. The spectra of CO at this pressure and at the subsequent outgassing steps were collected at a resolution of 4 cm^{-1} with a Bruker Equinox 55 spectrometer, equipped with a MCT detector. The number of scans was adjusted to 128 to attain a good signal-to-noise ratio. The data were normalized to the 'optical density' (weight of pellet in mg / area of pellet in cm^2) in order to make differences in intensity independent of differences in the thickness of the pellets [28]. Spectra of adsorbed CO are reported in absorbance, after subtraction of the spectra of the sample before CO admission.

2.2.7 Electrochemical measurements. To perform the electrochemical measurements the materials were packed into carbon paste electrodes. Electrodes were prepared by accurate hand-mixing of highly viscous mineral oil (0.175 g) with graphite powder (0.250 g) and HA nanoparticles (0.075 g). Besides, a control electrode without HA nanoparticles was prepared following the same procedure: highly viscous mineral oil (0.175 g) and graphite powder (0.325 g). In all the cases, components were homogenized to obtain a mixture that was subsequently packed into a piston-driven carbon paste holder [29]. Whenever needed, the surface of carbon paste (with diameter of 2 mm) was mechanically renewed by extruding ca. 0.5 mm carbon paste out of the electrode holder and smoothing with a wet filter paper.

Cyclic voltammetry (CV) measurements were carried out with an Autolab electrochemical analyzer operated *via* NOVA 2.14 software (Metrohm Autolab, Utrecht, The Netherlands). The conventional three-electrode configuration with the different HA nanoparticles carbon paste electrode was employed throughout the work. The Ag/AgCl 3 M KCl and a Pt wire served as the reference and auxiliary electrodes, respectively. All electrochemical experiments were carried out in one-compartment voltammetric cell (10-20 mL) at room temperature. CV measurements were performed in 10 mL of 0.02 M PBS buffer. The catalytic activity of the HA nanoparticles was tested by addition of H_2O_2 that was prepared in PBS buffer with a concentration of 0.1 M. All carbon paste electrodes were kept for one day after their preparation to homogenize.

3. Results and Discussion

3.1. Elemental and Structural Analysis

The elemental composition of the samples is presented in Table 1. The SSA of all samples is in order of magnitude expected for nanometric materials (125 m^2/g) and does not show significant differences after the exchange procedure.

In all cases, the exchange between Cu^{2+} and Ca^{2+} cations was achieved. It can be noticed that the difference in copper incorporated between HA_Cu_0.05 and HA_Cu_0.1 is minimal, being 7.2 and 7.7 (wt. %), respectively. As it was reported before [30, 31], this could be the consequence of reaching the saturation of the surface cations exchange capacity, which in our conditions is achieved already when the sample is put in contact with a 0.05 M Cu^{2+} solution. Indeed, ICP analysis of the supernatant solutions after the exchange procedure highlights that the Cu uptake is almost 100 % for the 0.01 M copper nitrate solution, while is only ~ 40 % for the 0.05 M solution (see Table S1 in the supplementary material), suggesting a saturation of the HA exchange capability.

The content of phosphorous is the same for all the materials since it is not involved in the cation exchange mechanism. Conversely, as can be expected, the Ca/P atomic ratios in the exchanged materials are noticeably lower than in the HA, owing to the substitution of the surface-exposed Ca^{2+} cations with Cu^{2+}. This is in agreement with the almost constant value of the (Ca+Cu)/P atomic ratio of the samples, which is close to the stoichiometric value of HA (1.67), indicating the consistency of the Ca→Cu surface exchange. These evidences suggest that other possible mechanisms reported in literature for HA synthesized at higher temperatures (and thus more crystalline), involving Cu^{2+} complexation with surface anions [22], are not dominant in our case, where the higher reactivity given by the lower HA crystallinity allows Ca^{2+} cations to detach from HA surface and be exchanged with Cu^{2+}. This statement is further confirmed by the ICP analysis of the solution after the exchange procedure (see Table S1 in the supplementary material) which highlights an almost perfect 1:1 exchange between Cu^{2+} and Ca^{2+} for HA_Cu_0.01, paired with a negligible phosphate release. However, it is worth to note that the small increase of the (Ca+Cu)/P atomic ratio from 1.67 to 1.70 could also be compatible with the coexistence of a small contribution from a surface complexation mechanism for the samples with higher Cu loadings, as proposed for more crystalline samples by Campisi et al [22]. This possibility is also supported by the slightly higher (1.5) ratio between uptaken Cu^{2+} and released Ca^{2+} for HA_Cu_0.1 (see last column of Table S1).

On the basis of these data the number of Cu^{2+} cations exposed per area unit was estimated. The calculated value for HA_Cu_0.05 and HA_Cu_0.1 slightly exceeds the surface density of Ca ions in pure HA reported in previous studies (4.5 Ca^{2+}/nm^2) [10, 32], which implies the maximum possible exchange of the surface-exposed Ca atoms to Cu. The discrepancy between the surface density of exposed cations

for pure HA and estimated amount of Cu ions on the surface of the exchanged materials could be possibly explained by the presence of a limited exchange also of the sub-surface or bulk Ca^{2+} ions. It is worth noticing that the amount of Cu in the HA_Cu_0.01 sample (1.6 Cu^{2+}/nm^2) is considerably lower than the amount of Ca in HA suggesting the co-existence of both Ca and Cu ions on its surface.

Table 1. Samples codes, weight percent composition measured by ICP, atomic ratios and estimated number of Cu^{2+} cations per nm^2.

Sample	$[Ca^{2+}]$ (%wt.)	$[Cu^{2+}]$ (%wt.)	[P] (%wt.)	Ca/P	(Ca+Cu)/P	Cu^{2+}/nm^2
HA	33.0 ± 0.7	-	15.3 ± 0.3	1.67 ± 0.04	-	-
HA_Cu_0.01	33.2 ± 0.1	2.09 ± 0.03	16.0 ± 0.1	1.60 ± 0.01	1.67 ± 0.01	1.6
HA_Cu_0.05	29.0 ± 0.2	7.67 ± 0.02	15.5 ± 0.1	1.45 ± 0.01	1.69 ± 0.01	5.8
HA_Cu_0.1	28.4 ± 0.2	7.17 ± 0.09	15.0 ± 0.2	1.46 ± 0.02	1.70 ± 0.02	5.4

Structural characterization of the samples was obtained from the XRD patterns (Figure 1), which show broad diffraction peaks indexed as hydroxyapatite single phase (PDF no. 00-009-0432). There are no marked differences between the copper loaded samples and the pristine material.

A more quantitative analysis, reported in Table 2, of HA unit cell parameters shows no significant differences between the samples, confirming that the copper exchange has occurred mainly on the surface and, in part, in the bulk without altering the crystal structure. From the estimation of crystalline domains along the *c*-axis ($D_{(002)}$) and *a-b* plane ($D_{(310),}$) it can be observed that all samples have comparable crystalline domain dimensions and have a high $D_{(002)}/D_{(310)}$ ratio, in agreement with the elongated morphology which preferentially show {010} facets as already reported in previous studies [7]. Furthermore, it can be observed that copper-exchanged samples have a slightly shorter $D_{(002)}$ size, suggesting that a slight decrease in crystallinity occurs during the process. This is likely due to the acidic pH (4.8-4.0) of the solution during the exchange procedure (see Experimental Section). However, soaking the HA samples in acidic solutions at the same pH, but in absence of copper nitrate, results in a very limited Ca and P release (see Table S1 in the supplementary material) confirming that ion exchange was the most relevant mechanism during the doping process. Moreover, in the patterns of the HA_Cu_0.05 and HA_Cu_0.1 samples, an additional small peak appears at 12° ascribed to the precipitation of a small fraction (< 1% wt) of brushite ($CaHPO_4 \cdot 2H_2O$, PDF no. 09-0077), which is a calcium phosphate phase more stable in acidic conditions.

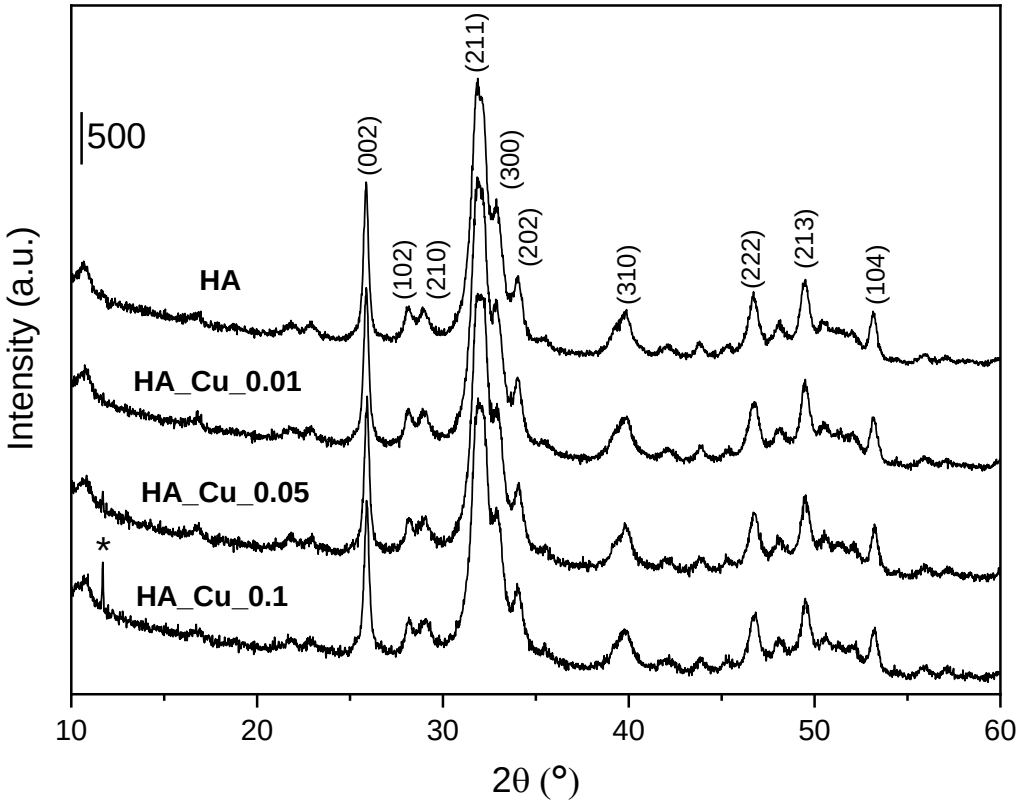

Figure 1. XRD patterns of the pure and copper-exchanged HAs with indexing of the main diffraction peaks. The diffraction peak associated with the brushite phase is marked with an asterisk.

Table 2. Unit cell parameters and crystalline domains along the [002] and [310] directions obtained from the XRD patterns of the samples.

Sample	*a* (Å)	*c* (Å)	$D_{(002)}$ (nm)	$D_{(310)}$ (nm)	$D_{(002)}/D_{(310)}$
HA	9.427 ± 0.002	6.895 ± 0.001	39 ± 1	12 ± 1	3.2
HA_Cu_0.01	9.423 ± 0.002	6.890 ± 0.001	35 ± 1	11 ± 1	3.3
HA_Cu_0.05	9.426 ± 0.002	6.891 ± 0.001	36 ± 1	11 ± 1	3.2
HA_Cu_0.1	9.425 ± 0.002	6.891 ± 0.001	36 ± 1	9 ± 1	4.0

More detailed structural information about the materials was obtained by solid-state NMR (ss-NMR). Figure 2 shows the ^{1}H MAS NMR and ^{1}H ECHO NMR spectra of the samples. The ECHO NMR experiment, with appropriate delay time, has been performed as an optimized compromise between the signal decay owing to relaxation and the resolution gain owing to longer delay times [33]. Spectral parameters extracted from these data are summarized in Table 3. The HA sample consists of two intense resonances at -0.1 and 5.2 ppm (Figure 2A) due to apatite structural hydroxyl groups and surface-adsorbed water, respectively [34]. In addition, low intensity peaks due to hydroxyls on calcium in the HA surface layers are detected at 1.2 and 0.8 ppm [35].

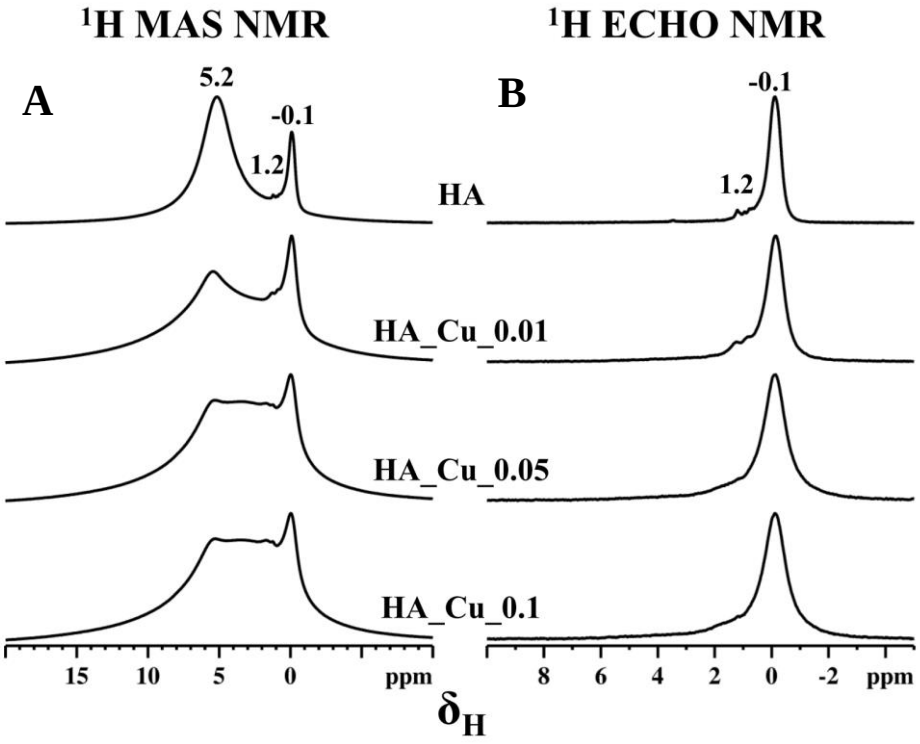

Figure 2. ^{1}H MAS NMR (A) and ^{1}H ECHO NMR (B) spectra of HA samples recorded with a MAS rate of 15 kHz.

Table 3. ^{1}H and ^{31}P NMR chemical shifts δ (±0.05 ppm) and linewidths Δ (±10 Hz) of selected species observed in HA samples. δ_H = -0.1 ppm corresponds to apatite structural hydroxyls and δ_P = 2.7 ppm to bulk phosphate groups.

Sample	δ_H (ppm)	Δ (Hz)	δ_P (ppm)	Δ (Hz)
HA	-0.1	227	2.7	308
HA_Cu_0.01	-0.1	356	2.7	356
HA_Cu_0.05	-0.1	470	2.7	389
HA_Cu_0.10	-0.1	489	2.7	390

After the copper exchange, the chemical shifts of peaks associated to structural hydroxyls and surface-adsorbed water remain unaffected, while the resonances appear significantly broadened, especially for water, depending on the extent of Cu loading. This broadening suggests that water molecules can be complexed by the Cu sites. The most striking feature of Figure 2A is the observation of a very broad peak centered at around 3 ppm in copper-exchanged samples, which is tentatively assigned to Cu-OH species. The linewidth of all peaks (in Hz) increases with increasing Cu loading (Table 3) and this effect is attributed to the presence of paramagnetic Cu ions on the apatite surface [36, 37]. Compared to the spectrum of the HA, the spectra of Cu loaded samples are significantly unresolved revealing substantially greater line broadening and thus being assignable only in part. However, a detailed inspection of full width at half-maximum (FWHM) extracted from ^{1}H ECHO NMR data (Figure 2B and Table 3) on structural hydroxyls reveals the manifestation of the line broadening associated to increased Cu loading in apatite samples.

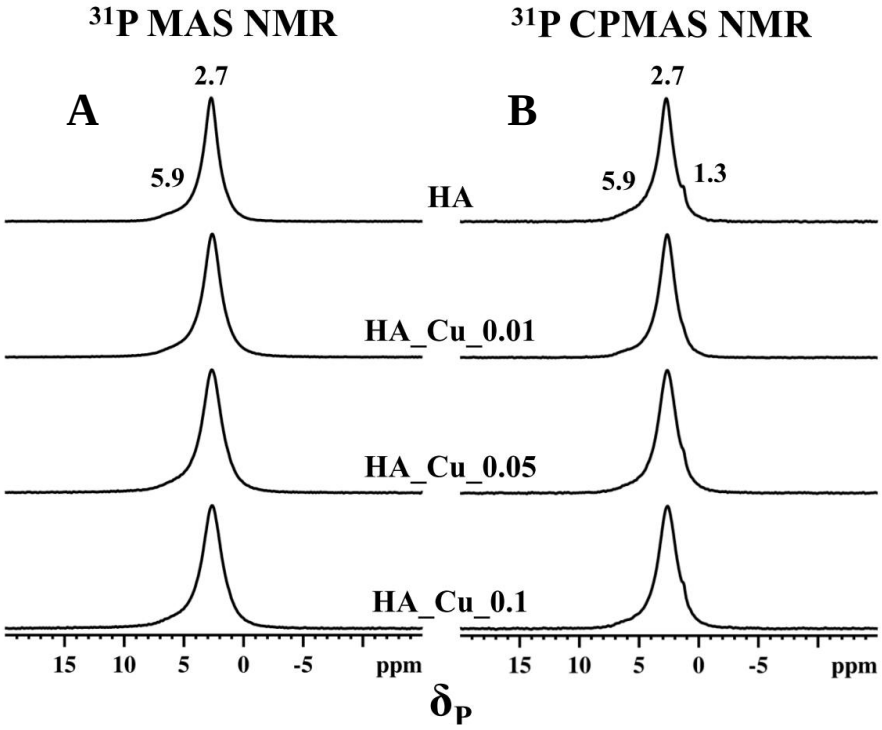

Figure 3. ^{31}P solid-state NMR spectra of the HA samples recorded using MAS (A) and CPMAS (B) under proton decoupling conditions.

The ^{31}P MAS and CPMAS NMR spectra of the HA samples are shown in Figure 3. The MAS NMR spectrum of HA, recorded under proton decoupling, reveals two resonances, one at 2.7 ppm attributable to the crystallographically equivalent bulk phosphate groups and the second one at 5.9 ppm due to surface phosphate groups [38, 39]. However, the ^{31}P CPMAS NMR spectrum of the same sample showed an

additional resonance at 1.3 ppm and is due to surface HPO_4^{2-} groups [39] (Figure 3A). The appearance of a peak in a CPMAS spectrum reveals the strong ^{1}H-^{31}P heteronuclear dipolar interaction, whose strength decreases with increasing internuclear distance [40]. The ^{31}P CPMAS NMR spectra of copper-exchanged samples are essentially identical in terms of chemical shifts, however, a progressive increase in linewidth of peaks with increasing Cu loading is noted due to dipole-dipoles interactions between Cu electron spin and nuclear spins (^{1}H or ^{31}P) leading to a faster nuclear spin relaxation behaviour (Table 3). This results in significantly less-well resolved spectra, therefore, substantially greater line broadening. However, the presence of three resonances in copper-exchanged samples can be confirmed from the spectral deconvolution. The ss-NMR data further confirm the substitution of surface Ca^{2+} ions with Cu^{2+} also involving the sub-surface or bulk layers for the HA samples with higher loadings.

Finally, it is worth noting that the combined elemental analysis and structural characterization showed that the HA_Cu_0.05 and HA_Cu_0.1 samples are comparable. Therefore, we can conclude that the complete substitution of surface Ca^{2+} ions with Cu^{2+} occurs already with the 0.05 M $Cu(NO_3)_2$ solution. On this basis, we will not further discuss the HA_Cu_0.1 sample in the following sections.

3.2. Surface characterization

To investigate the surface properties of the materials by infrared spectroscopy, we selected carbon monoxide, which is a versatile probe molecule, able to study both Ca and Cu surface sites. Before performing CO adsorption experiments, the surface of the materials should be ’cleaned‘ from residual water molecules adsorbed on the surface [41, 42]. To achieve this objective, the HA materials need to be pre-outgassed at 423 K for 2 hours. The efficiency of this protocol into attaining a ’clean‘ surface without introducing significant structural modifications was demonstrated elsewhere [7].

The sets of spectra collected at 100 K at decreasing CO coverages for HA, HA_Cu_0.01 and HA_Cu_0.05 samples are shown in Figure 4. In HA sample (Figure 4A) an intense band centered at 2168 cm^{-1} was observed, which progressively shifts to 2178 cm^{-1} while decreasing the CO coverage. This signal is related to the ν(CO) mode of carbon monoxide molecules adsorbed on surface-exposed Ca^{2+} cations of HA [7, 10]. At lower wavenumbers (around 2143 cm^{-1}) at the highest CO coverage, the CO gas phase profile can be appreciated, due to the high pressure into the IR cell, witnessing that the material is completely covered by CO molecules.

In the copper-exchanged samples HA_Cu_0.01 (Figure 4B) and HA_Cu_0.05 (Figure 4 C), new ν(CO) bands appear that are due to the presence of Cu ions on the surface of the materials: one in the range 2105-2120 cm^{-1}, and another one in the range 2150-2160 cm^{-1}. It can be observed that the most intense band for both copper-containing samples is centered at lower wavenumbers (2108 cm^{-1} in the case of HA_Cu_0.01, and at 2115 cm^{-1} in the case of HA_Cu_0.05). In both cases, a shift of these bands towards

higher wavenumbers at decreasing coverage is observed, owing to the progressive fading out of CO-CO lateral interactions [43]. Considering the position of the bands and the bond strength between the CO and the copper ions, evaluated by the irreversibility of the bond at room temperature, this lower wavenumber band was attributed to Cu^{+} cations [44, 45]. The presence of Cu^{+} cations in the material can be explained by a partial reduction of Cu^{2+} surface ions occurring during the heating procedure in vacuum conditions [46], performed before the CO adsorption experiment.

The second band, found at higher wavenumbers (2149/2155 cm^{-1}), shows a lower intensity and a lower stability since it totally disappears during the outgassing procedure at beam temperature. For these reasons, this signal can be attributed, on the basis of previous literature assignments [44], to CO interacting with Cu^{2+} cations not reduced during the activation process. It is also worth to note that, in the case of HA_Cu_0.01, the band 2149 cm^{-1} is overlapped with a signal at 2166 cm^{-1} due to CO adsorbed on residual Ca^{2+} cations on the HA surface. Conversely, in the spectra of CO adsorbed on HA_Cu_0.05, the 2166 cm^{-1} component is absent, further confirming the complete exchange of the surface-exposed Ca cations with Cu.

To further confirm these assignments, we performed an IR experiment adding an oxidation step after the outgassing procedure at 423 K. As visible in Figure S1 of the supplementary material, the relative intensity of the Cu^{+} signal is considerably reduced in favor of the band assigned to CO adsorbed on Cu^{2+} cations. The observed different reducibility of the Cu^{2+} could likely be ascribed to cations located in different positions in the HA (e.g. resulting from surface exchange or from surface complexation).

Finally, also surface P-OH can act as adsorption sites for CO, giving rise to a band at about 2170 cm^{-1}. Indeed, from the insets of Figure 4 we can notice a perturbation of the ν(OH) mode of the P-OH groups, which is initially centered at ~ 3680 cm^{-1}, and it is then downshifted after CO adsorption. However, given the small intensity of the P-OH band and considering the ratio between the integrated intensity of the ν(OH) band of unperturbed P-OH and that expected for the stretching band of CO adsorbed on them [7], we can conclude that the interaction of CO with P-OH groups contributes into a limited extent to the signal in the ν(CO) spectral region.

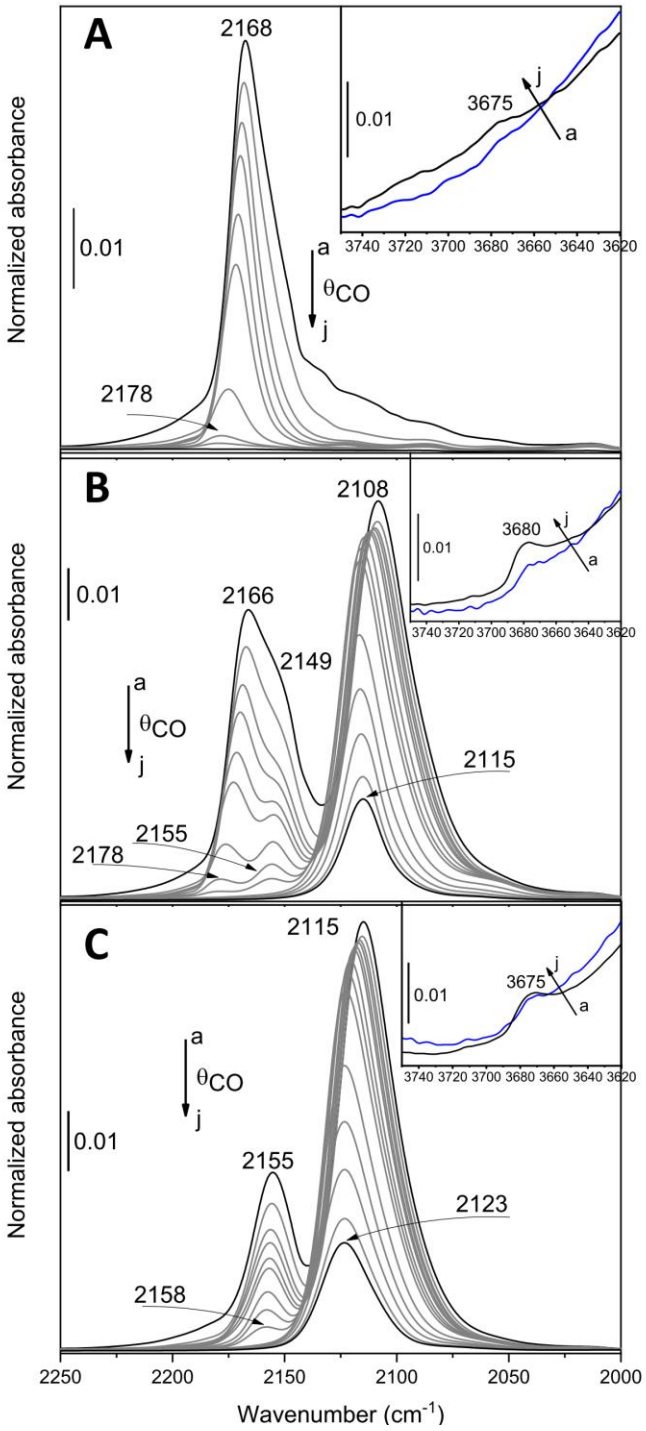

Figure 4. FTIR spectra of CO adsorbed at ca. 100 K on HA (panel A), HA_Cu_0.01 (panel B) and HA_Cu_0.05 (panel C) at different coverages starting from 50 mbar (curves a) with stepwise outgassing till 1×10^{-3} mbar (curves j). The spectrum of the activated material has been subtracted from all spectra. In the inset the OH stretching region is reported.

3.3. Electrocatalytic H_2O_2 reduction

The potential catalytic activity of HA and HA_Cu samples was investigated by Cyclic Voltammetry (CV) toward the electrochemical reduction of H_2O_2. Figure 5A shows the voltammograms obtained for

the bare electrode (black curves) in comparison with the sample HA_Cu_0.05 (red curves), scanning the applied potential from 1 to -1.4 V. An analogous methodology has been adopted for all the samples. The CV of the different electrodes in the PBS buffer was first recorded, then a solution of H_2O_2 with a final concentration of 0.2 mM was added to the cell and the voltammetry was repeated. In the latter case, we can appreciate an evident increase of cathodic current for sample HA_Cu_0.05 as a broad peak that starts from −0.4 V and extends down to −1.4 V, due to the H_2O_2 electrochemical reduction. Moreover, in the voltammogram of HA_Cu_0.05 we can see a small oxidation peak around 0.0 V: this signal can be due to the re-oxidation of the copper species in the electrode [47].

Figure 5B shows the differences in current intensity in absolute value (|ΔI|), calculated at -0.4 V, between the voltammograms before and after addition of H_2O_2 for each sample. The shift of the H_2O_2 reduction potential to less negative values in such a way that at −0.4 V the cathodic current is significantly higher than that of bare electrode is interesting for practical applications when compared to other copper-based systems reported in literature [48, 49]. Indeed, in electroanalysis the possibility to operate at low potentials is crucial to achieve higher selectivity, avoiding the interferences which could be present in a real complex sample at higher applied potentials due to other species which can undergo electrochemical oxidation/reduction. Paying attention to the differences in |ΔI|, it can be observed that the bare electrode and HA have a comparable catalytic activity. On the contrary, for HA_Cu_0.01, a small increment of the catalytic activity is observed, which can be attributed to the incorporation of Cu^{2+} cations into the surface of the HA. The current increase is much more evident for the sample HA_Cu_0.05, confirming that the catalytic activity of the samples increases with the amount of Cu^{2+} cations incorporated into the surface. This is in agreement with previous reports which highlighted that copper ions induce catalytic activity toward electrochemical reduction of H_2O_2 [27]. We can conclude that our materials behave like nanozymes, i.e. nanomaterials that mimic enzyme-like catalytic activity [49], mimicking in our case the catalase enzyme.

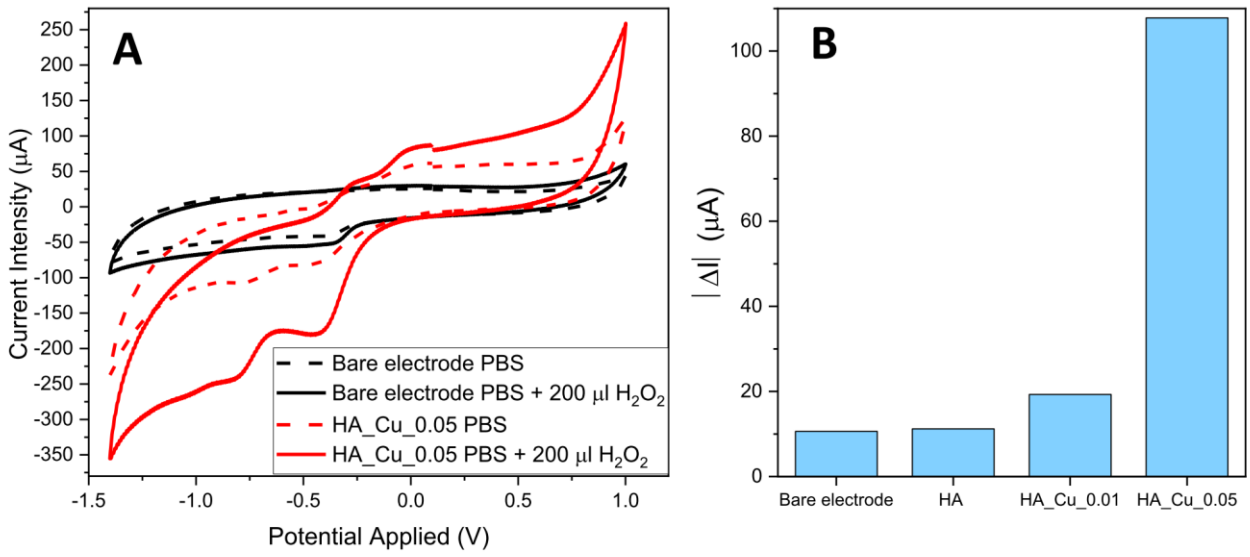

Figure 5. (A) Comparison between the voltammograms of bare electrode (black) and HA_Cu_0.05 (red) in PBS (dashed curves) and after addition of H_2O_2 with a final concentration in the cell of 0.2 mM (solid lines). (B) Differences in current intensity in absolute value (|ΔI|), calculated at -0.4 V, between the voltammograms before and after addition of H_2O_2 for each sample.

4. Conclusions

In this study we synthesized HA nanoparticles with high specific surface area (125 m^2/g), showing elongated {010} facets. The synthesis was optimized to obtain HA surfaces with high concentration of Ca^{2+} and low crystallinity to favor surface ion exchange. The HA samples were then soaked in copper (II) solutions at different concentrations (i.e. 0.01, 0.05 and 0.1 M). We found that the complete substitution of surface Ca^{2+} with Cu^{2+} cations can be already achieved with the 0.05 M solution. Increasing the concentration of the solution does not result in a higher Cu content in the final material, which remains ~ 7 %wt. For the HA_Cu_0.01 sample, where the substitution of surface Ca^{2+} was not complete, we obtained an almost perfect 1:1 exchange between the available Cu^{2+} in solution and surface Ca^{2+}, paired with a negligible phosphate release. Conversely, a small contribution from a surface complexation mechanism could also be present for the samples with higher Cu loadings.

Combining XRD and solid-state NMR, we highlighted that the copper exchange took place mainly at the surface and, for the higher Cu concentrations, also in the sub-surface/bulk layers, without significantly altering HA crystal structure. However, a slight decrease in crystallinity occurred for copper-containing samples, likely due to the acidic pH of the copper solution used during the exchange procedure. Moreover, we observed the appearance in the ^1H MAS NMR spectra of copper-exchanged samples of a very broad peak, centered at around 3 ppm, which could be assigned to the formation of Cu-OH species.

The surface properties of the materials were investigated by FTIR spectroscopy of adsorbed CO after activating the samples at 423 K. On the HA_Cu_0.01 sample, carbon monoxide was able to probe both Ca and Cu cations, while only bands related to Cu^{2+}/Cu^{+} sites were observed on the HA_Cu_0.05 sample, further confirming the complete surface exchange of Ca with Cu.

Finally, a preliminary test of the electrocatalytic activity of the material was performed by cyclic voltammetry. Moving from the pristine HA to HA_Cu_0.01 and HA_Cu_0.05 samples, we observed a progressive increase in catalytic activity toward the electrochemical reduction of H_2O_2, which could pave the way to future applications of copper-exchanged HA materials as an alternative to noble metal and enzyme catalysts for electrochemical H_2O_2 sensors.

Declaration of Competing Interest. The authors declare that they have no known competing financial interests or personal relationships that could have appeared to influence the work reported in this paper.

CRediT authorship contribution statement. Guillermo Escolano Casado: Investigation, Data Curation, Writing - Original Draft; Pavlo Ivanchenko: Writing - Review & Editing, Data Curation; Geo Paul: Investigation, Data Curation, Writing - Review & Editing; Chiara Bisio: Supervision, Writing - Review & Editing; Leonardo Marchese: Funding acquisition; Amir M. Ashrafi: Investigation, Writing - Review & Editing; Vedran Milosavljevic: Writing - Review & Editing; Lorenzo Degli Esposti: Investigation, Formal analysis, Writing - Review & Editing; Michele Iafisco: Writing - Review & Editing, Supervision, Conceptualization; Lorenzo Mino: Supervision; Writing – Original Draft; Data Curation; Conceptualization.

References

[1] J. Gomez-Morales, M. Iafisco, J.M. Delgado-Lopez, S. Sarda, C. Drouet, Progress on the preparation of nanocrystalline apatites and surface characterization: Overview of fundamental and applied aspects, Prog. Cryst. Growth Charact. Mater. 59 (2013) 1-46.

[2] R. Rial, M. Gonzalez-Durruthy, Z. Liu, J.M. Ruso, Advanced Materials Based on Nanosized Hydroxyapatite, Molecules 26 (2021) 3190.

[3] A. Fihri, C. Len, R.S. Varma, A. Solhy, Hydroxyapatite: A review of syntheses, structure and applications in heterogeneous catalysis, Coord. Chem. Rev. 347 (2017) 48-76.

[4] G.B. Ramirez-Rodriguez, G. Dal Sasso, F.J. Carmona, C. Miguel-Rojas, A. Perez-de-Luque, N. Masciocchi, A. Guagliardi, J.M. Delgado-Lopez, Engineering Biomimetic Calcium Phosphate Nanoparticles: A Green Synthesis of Slow-Release Multinutrient (NPK) Nanofertilizers, ACS Appl. Bio Mater. 3 (2020) 1344-1353.

[5] H.Y. Yoon, J.G. Lee, L. Degli Esposti, M. Iafisco, P.J. Kim, S.G. Shin, J.R. Jeon, A. Adamiano, Synergistic Release of Crop Nutrients and Stimulants from Hydroxyapatite Nanoparticles Functionalized with Humic Substances: Toward a Multifunctional Nanofertilizer, ACS Omega 5 (2020) 6598-6610.

[6] M. Ibrahim, M. Labaki, J.M. Giraudon, J.F. Lamonier, Hydroxyapatite, a multifunctional material for air, water and soil pollution control: A review, J. Hazard. Mater. 383 (2020) 18.

[7] Y. Sakhno, P. Ivanchenko, M. Iafisco, A. Tampieri, G. Martra, A Step toward Control of the Surface Structure of Biomimetic Hydroxyapatite Nanoparticles: Effect of Carboxylates on the {010} P-Rich/Ca-Rich Facets Ratio, J. Phys. Chem. C 119 (2015) 5928-5937.

[8] C.A. Ospina, J. Terra, A.J. Ramirez, M. Farina, D.E. Ellis, A.M. Rossi, Experimental evidence and structural modeling of nonstoichiometric (010) surfaces coexisting in hydroxyapatite nano-crystals, Colloid Surf. B-Biointerfaces 89 (2012) 15-22.

[9] G. Molino, M.C. Palmieri, G. Montalbano, S. Fiorilli, C. Vitale-Brovarone, Biomimetic and mesoporous nano-hydroxyapatite for bone tissue application: a short review, Biomed. Mater. 15 (2020) 022001.

[10] L. Bertinetti, A. Tampieri, E. Landi, C. Ducati, P.A. Midgley, S. Coluccia, G. Martra, Surface structure, hydration, and cationic sites of nanohydroxyapatite: UHR-TEM, IR, and microgravimetric studies, J. Phys. Chem. C 111 (2007) 4027-4035.

[11] K. Kandori, A. Fudo, T. Ishikawa, Study on the particle texture dependence of protein adsorption by using synthetic micrometer-sized calcium hydroxyapatite particles, Colloid Surf. B-Biointerfaces 24 (2002) 145-153.

[12] S.C. Oh, J.Y. Xu, D.T. Tran, B. Liu, D.X. Liu, Effects of Controlled Crystalline Surface of Hydroxyapatite on Methane Oxidation Reactions, ACS Catal. 8 (2018) 4493-4507.

[13] C. Wen, Y.Y. Cui, X. Chen, B.N. Zong, W.L. Dai, Reaction temperature controlled selective hydrogenation of dimethyl oxalate to methyl glycolate and ethylene glycol over copper-hydroxyapatite catalysts, Appl. Catal. B-Environ. 162 (2015) 483-493.

[14] Z.P. Qu, Y.H. Sun, D. Chen, Y. Wang, Possible sites of copper located on hydroxyapatite structure and the identification of active sites for formaldehyde oxidation, J. Mol. Catal. A-Chem. 393 (2014) 182-190.

[15] Y. Masuyama, K. Yoshikawa, N. Suzuki, K. Hara, A. Fukuoka, Hydroxyapatite-supported copper(II)-catalyzed azide-allcyne 3+2 cycloaddition with neither reducing agents nor bases in water, Tetrahedron Lett. 52 (2011) 6916-6918.

[16] J. Jemal, H. Tounsi, K. Chaari, C. Petitto, G. Delahay, S. Djemel, A. Ghorbel, NO reduction with NH_3 under oxidizing atmosphere on copper loaded hydroxyapatite, Appl. Catal. B-Environ. 113 (2012) 255-260.

[17] S. Campisi, M.G. Galloni, F. Bossola, A. Gervasini, Comparative performance of copper and iron functionalized hydroxyapatite catalysts in NH_3-SCR, Catal. Commun. 123 (2019) 79-85.

[18] V. Stanic, S. Dimitrijevic, J. Antic-Stankovic, M. Mitric, B. Jokic, I.B. Plecas, S. Raicevic, Synthesis, characterization and antimicrobial activity of copper and zinc-doped hydroxyapatite nanopowders, Appl. Surf. Sci. 256 (2010) 6083-6089.

[19] M. Othmani, H. Bachoua, Y. Ghandour, A. Aissa, M. Debbabi, Synthesis, characterization and catalytic properties of copper-substituted hydroxyapatite nanocrystals, Mater. Res. Bull. 97 (2018) 560-566.

[20] A.S. Karpov, J. Nuss, M. Jansen, P.E. Kazin, Y.D. Tretyakov, Synthesis, crystal structure and properties of calcium and barium hydroxyapatites containing copper ions in hexagonal channels, Solid State Sci. 5 (2003) 1277-1283.

[21] M.A. Zykin, A.V. Vasiliev, L.A. Trusov, R.E. Dinnebier, M. Jansen, P.E. Kazin, Solid state solubility of copper oxides in hydroxyapatite, J. Solid State Chem. 262 (2018) 38-43.

[22] S. Campisi, C. Castellano, A. Gervasini, Tailoring the structural and morphological properties of hydroxyapatite materials to enhance the capture efficiency towards copper(ii) and lead(ii) ions, New J. Chem. 42 (2018) 4520-4530.

[23] P. Kanchana, N. Lavanya, C. Sekar, Development of amperometric L-tyrosine sensor based on Fe-doped hydroxyapatite nanoparticles, Mater. Sci. Eng. C-Mater. Biol. Appl. 35 (2014) 85-91.

[24] R. Mirzajani, S. Karimi, Preparation of gamma-Fe_2O_3/hydroxyapatite/Cu(II) magnetic nanocomposite and its application for electrochemical detection of metformin in urine and pharmaceutical samples, Sens. Actuator B-Chem. 270 (2018) 405-416.

[25] E. Iyyappan, S.J.S. Justin, P. Wilson, A. Palaniappan, Nanoscale Hydroxyapatite for Electrochemical Sensing of Uric Acid: Roles of Mesopore Volume and Surface Acidity, ACS Appl. Nano Mater. 3 (2020) 7761-7773.

[26] W. Chen, S. Cai, Q.Q. Ren, W. Wen, Y.D. Zhao, Recent advances in electrochemical sensing for hydrogen peroxide: a review, Analyst 137 (2012) 49-58.

[27] M. Sys, A. Mukherjee, G. Jashari, V. Adam, A.M. Ashrafi, M. Novak, L. Richtera, Bis(2,2 '-bipyridil)Copper(II) Chloride Complex: Tyrosinase Biomimetic Catalyst or Redox Mediator?, Materials 14 (2021) 113.

[28] L. Mino, L. Mandrile, L. Iannarelli, C. Portesi, G. Martra, A.M. Rossi, Characterization of Nanoparticles: Measurement Processes for Nanoparticles, Elsevier, 2019, pp. 457-480.

[29] K.V. I. Švancara, R. Metelka, Czech Patent CZ 301714 B6, Int. Cl. G01N 27/30 (applied 2 Dec 2002, administered 22 Apr 2010).

[30] O. Rosskopfova, M. Galambos, J. Ometakova, M. Caplovicova, P. Rajec, Study of sorption processes of copper on synthetic hydroxyapatite, J. Radioanal. Nucl. Chem. 293 (2012) 641-647.

[31] L. Yang, W.H. Zhong, J. Cui, Z.G. Wei, W. Wei, Enhanced Removal of Cu(II) Ions from Aqueous Solution by Poorly Crystalline Hydroxyapatite Nanoparticles, J. Dispersion Sci. Technol. 37 (2016) 956-968.

[32] Y. Sakhno, L. Bertinetti, M. Iafisco, A. Tampieri, N. Roveri, G. Martra, Surface Hydration and Cationic Sites of Nanohydroxyapatites with Amorphous or Crystalline Surfaces: A Comparative Study, J. Phys. Chem. C 114 (2010) 16640-16648.

[33] G. Paul, G.E. Musso, E. Bottinelli, M. Cossi, L. Marchese, G. Berlier, Investigating the Interaction of Water Vapour with Aminopropyl Groups on the Surface of Mesoporous Silica Nanoparticles, ChemPhysChem 18 (2017) 839-849.

[34] J.P. Yesinowski, H. Eckert, Hydrogen environments in calcium phosphates: ^{1}H MAS NMR at high spinning speeds, J. Am. Chem. Soc. 109 (1987) 6274-6282.

[35] G. Paul, E. Boccaleri, C. Cassino, D. Gastaldi, L. Buzzi, F. Canonico, L. Marchese, Fingerprinting the Hydration Products of Hydraulic Binders Using Snapshots from Time-Resolved In Situ Multinuclear MAS NMR Spectroscopy, J. Phys. Chem. C 125 (2021) 9261-9272.

[36] A. Bhattacharjee, Y.A. Fang, T.J.N. Hooper, N.L. Kelly, D. Gupta, K. Balani, I. Manna, T. Baikie, P.T. Bishop, T.J. White, J.V. Hanna, Crystal Chemistry and Antibacterial Properties of Cupriferous Hydroxyapatite, Materials 12 (2019) 17.

[37] A.J. Pell, G. Pintacuda, C.P. Grey, Paramagnetic NMR in solution and the solid state, Prog. Nucl. Magn. Reson. Spectrosc. 111 (2019) 1-271.

[38] T. Isobe, S. Nakamura, R. Nemoto, M. Senna, H. Sfihi, Solid-state double nuclear magnetic resonance study of the local structure of calcium phosphate nanoparticles synthesized by a wet-mechanochemical reaction, J. Phys. Chem. B 106 (2002) 5169-5176.

[39] M. Jarlbring, D.E. Sandstrom, O.N. Antzutkin, W. Forsling, Characterization of active phosphorus surface sites at synthetic carbonate-free fluorapatite using single-pulse ^{1}H, ^{31}P, and ^{31}P CP MAS NMR, Langmuir 22 (2006) 4787-4792.

[40] G. Paul, C. Bisio, I. Braschi, M. Cossi, G. Gatti, E. Gianotti, L. Marchese, Combined solid-state NMR, FT-IR and computational studies on layered and porous materials, Chem. Soc. Rev. 47 (2018) 5684-5739.

[41] L. Mino, G. Spoto, S. Bordiga, A. Zecchina, Rutile Surface Properties Beyond the Single Crystal Approach: New Insights from the Experimental Investigation of Different Polycrystalline Samples and Periodic DFT Calculations, J. Phys. Chem. C 117 (2013) 11186-11196.

[42] L. Mino, C. Negri, R. Santalucia, G. Cerrato, G. Spoto, G. Martra, Morphology, Surface Structure and Water Adsorption Properties of TiO_2 Nanoparticles: A Comparison of Different Commercial Samples, Molecules 25 (2020) 4605.

[43] L. Mino, G. Spoto, S. Bordiga, A. Zecchina, Particles Morphology and Surface Properties As Investigated by HRTEM, FTIR, and Periodic DFT Calculations: From Pyrogenic TiO_2 (P25) to Nanoanatase, J. Phys. Chem. C 116 (2012) 17008-17018.

[44] K. Hadjiivanov, H. Knozinger, FTIR study of CO and NO adsorption and coadsorption on a Cu/SiO_2 catalyst: Probing the oxidation state of copper, Phys. Chem. Chem. Phys. 3 (2001) 1132-1137.

[45] J. Schumann, J. Krohnert, E. Frei, R. Schlogl, A. Trunschke, IR-Spectroscopic Study on the Interface of Cu-Based Methanol Synthesis Catalysts: Evidence for the Formation of a ZnO Overlayer, Top. Catal. 60 (2017) 1735-1743.

[46] V.L. Sushkevich, J.A. van Bokhoven, Revisiting copper reduction in zeolites: the impact of autoreduction and sample synthesis procedure, Chem. Commun. 54 (2018) 7447-7450.

[47] A.M. Ashrafi, K. Vytras, New procedures for voltammetric determination of copper (II) using antimony film-coated carbon paste electrodes, Electrochim. Acta 73 (2012) 112-117.

[48] M. Islam, N. Arya, P.G. Weidler, J.G. Korvink, V. Badilita, Electrodeposition of chitosan enables synthesis of copper/carbon composites for H_2O_2 sensing, Mater. Today Chem. 17 (2020) 10.

[49] A.M. Ashrafi, Z. Bytesnikova, J. Barek, L. Richtera, V. Adam, A critical comparison of natural enzymes and nanozymes in biosensing and bioassays, Biosens. Bioelectron. 192 (2021) 113494.